J. Fluid Mech. (2013), *vol.* 735, *pp.* 176–202. © Cambridge University Press 2013
doi:10.1017/jfm.2013.495

Cyclic flame propagation in premixed combustion

Philipp A. Boettcher[1,†], Shyam K. Menon[2], Brian L. Ventura[3], Guillaume Blanquart[2] and Joseph E. Shepherd[1]

[1]Graduate Aerospace Laboratories, California Institute of Technology, Pasadena, CA 91125, USA

[2]Mechanical Engineering, California Institute of Technology, Pasadena, CA 91125, USA

[3]Daniel Guggenheim School of Aerospace Engineering at the Georgia Institute of Technology, Atlanta, GA 30332, USA

(Received 30 October 2012; revised 16 August 2013; accepted 13 September 2013; first published online 23 October 2013)

In experiments of hot surface ignition and subsequent flame propagation, a puffing flame instability is observed in mixtures that are stagnant and premixed prior to ignition. By varying the size of the hot surface, power input, and combustion vessel volume, it was determined that the instability is a function of the interaction of the flame, with the fluid flow induced by the combustion products rather than the initial plume established by the hot surface. Pressure ranges from 25 to 100 kPa and mixtures of *n*-hexane/air with equivalence ratios between $\phi = 0.58$ and 3.0 at room temperature were investigated. Equivalence ratios between $\phi = 2.15$ and 2.5 exhibited multiple flame and equivalence ratios above $\phi = 2.5$ resulted in puffing flames at atmospheric pressure. The phenomenon is accurately reproduced in numerical simulations and a detailed flow field analysis revealed competition between the inflow velocity at the base of the flame and the flame propagation speed. The increasing inflow velocity, which exceeds the flame propagation speed, is ultimately responsible for creating a puff. The puff is then accelerated upward, allowing for the creation of the subsequent instabilities. The frequency of the puff is proportional to the gravitational acceleration and inversely proportional to the flame speed. A scaling relationship describes the dependence of the frequency on gravitational acceleration, hot surface diameter, and flame speed. This relation shows good agreement for rich *n*-hexane/air and lean hydrogen/air flames, as well as lean hexane/hydrogen/air mixtures.

Key words: buoyancy-driven instability, combustion, flames

1. Introduction

The process of thermal ignition of a flammable mixture by a hot surface and the subsequent flame propagation is important for the fundamental understanding of combustion as well as industrial safety applications. Of particular interest are flame instabilities arising in these situations as they affect the overall heat release rate. The

† Philipp Boettcher is currently an Assistant Research Professor at Drexel University's Mechanical Engineering and Mechanics Department. Email address for correspondence: philipp.boettcher@gmail.com

https://doi.org/10.1017/jfm.2013.495 Published online by Cambridge University Press

focus of this paper is on global flame instabilities, i.e. flickering or puffing flames, rather than small-scale instabilities at the flame front.

Flames exhibiting a flickering or puffing behaviour with frequencies around 10 Hz have been discussed since the First International Symposium on Combustion in September 1928 (Chamberlin & Rose 1948). The oscillation of non-premixed gaseous flames were investigated experimentally by Kimura (1965), Toong *et al.* (1965), Grant & Jones (1975) and Durao & Whitelaw (1974), and later by Tanoue *et al.* (2010). Theoretical work has been carried out by Buckmaster & Peters (1988), who investigated oscillations associated with the model problem of an infinite candle. Similar oscillations have also been observed in fires above pools of liquid fuels (Cetegen & Ahmed 1993) and in room fires (Zukoski 1986).

These oscillations are not limited to non-premixed flames, but can also occur in premixed flames as shown by Strawa & Cantwell (1989), Durox *et al.* (1990), Kostiuk & Cheng (1995), Cheng, Bédat & Kostiuk (1999), Shepherd, Cheng & Day (2005) and Guahk *et al.* (2009). In these studies, the frequency of the motion is also of the order of 10 Hz. In all of the previous experiments of premixed flames, the gaseous mixture was injected into the burner at a specific injection velocity. In contrast, the experiments and simulations presented here are performed in a combustible mixture which is quiescent prior to the ignition sequence.

The overall objective of the paper is to: (i) characterize the observed puffing phenomenon; (ii) determine its origin; and (iii) determine its relationship to fundamental properties of the fluid flame interaction. The following investigation of the cyclic flame propagation in a premixed environment is conducted using a combined experimental and numerical approach.

The paper first outlines the experimental and numerical methods used to study the premixed flames. Next, different regimes of flame propagation are identified as a function of the Richardson number, which changes as the mixture composition is varied. Third, the dependence of the puffing frequency on other parameters is explored and scaling laws are developed. Last, the detailed physics of the puffing phenomenon are examined and conclusions are drawn.

2. Experimental and numerical methods

The investigation of the cyclic flame propagation in a premixed environment is carried out using a combined experimental and numerical approach. This section presents details of these two approaches.

2.1. *Experimental setup and procedure*

The experimental setup consists of a high-temperature heat source located in the lower half of a closed-volume vessel (figure 1). Three different heat sources, namely a standard glow plug (Autolite 1110), a high-temperature glow plug (non-commercial Bosch 978801-0485), and a chromel wire, have been considered to investigate the effect of the hot surface size. The characteristic dimensions of the different hot surfaces as well as their power consumption are given in table 1. Similarly, two vessels of different sizes (2 and 22 l) were used to test the effects of vessel size and flow recirculation. Both combustion vessels are equipped with windows allowing for schlieren visualization of the ignition and subsequent flame propagation using a Phantom v710 high-speed camera. Typical frame rates are 1000–2000 frames per second (fps) using an 800×800 pixel resolution and an exposure time of $\sim$15 µs. In certain experiments, the excited CH^* radical, which emits between 420 and 440 nm, is

https://doi.org/10.1017/jfm.2013.495 Published online by Cambridge University Press

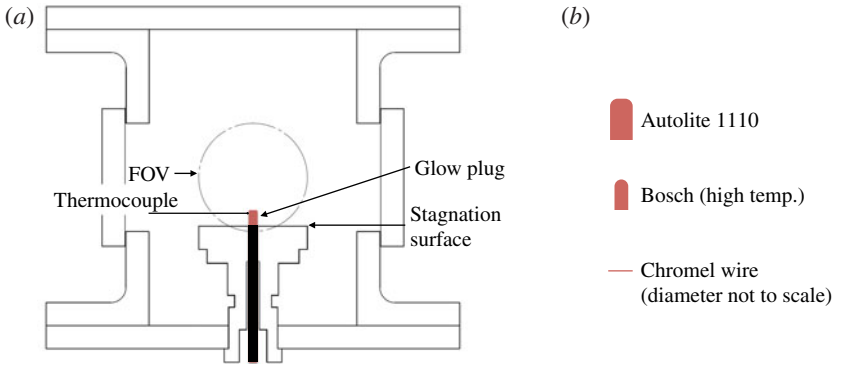


FIGURE 1. (Colour online) (*a*) Schematic of the Autolite 1110 glow plug mounted in the stagnation plate with the thermocouple reading the temperature at the hottest part of the glow plug. (*b*) Size comparison of the various hot surfaces used interchangeably in the location of the Autolite 1110 in (*a*); chromel wire diameter = 0.13 mm. The exact geometries of the glow plugs can be found in Boettcher (2012).

Hot surface (HS)	Power (W)	HS area (m^2)	Vessel volume (m^3)	Ign. temp. (K)	Puffing freq. (Hz)
Bosch glow plug[a]	≈100	8×10^{-5}	2×10^{-3}	920–975	12.5 ± 1
Autolite 1110 glow plug	96	1.5×10^{-4}	2×10^{-3}	775–825	12.5 ± 2
			22×10^{-3}	1120	14.5 ± 1
Chromel wire (dia. = 0.13 mm)	≈10	2.4×10^{-6}	2×10^{-3}	n/a[b]	14 ± 3

TABLE 1. The parameters changed for a fuel-rich hexane/air mixture ($\phi = 3.0$) were the power input to the hot surface, the area of the hot surface, and the volume of the vessel. The observed quantities were the minimum ignition temperature and the puffing frequency. [a] Non-commercial Bosch (961) 64 978801-0485 Duraterm. [b] Not available

observed by watching the flame through a narrow bandpass filter (centre wavelength $\lambda_c = 450 \pm 10$ nm, 70 ± 30 nm, full width at half-maximum) and a short-pass filter (transmittance >75 % in the range of $\lambda = 430$–500 nm).

For each experiment, the vessel is first evacuated and filled with a mixture of fuel (*n*-hexane and/or hydrogen), oxygen, and nitrogen to simulate combustion in air using the method of partial pressures (Dalton's law). The gas mixture is circulated for 2 min using either a mixer or a circulation pump. The mixture is given time to settle (another 2 min) such that the ignition sequence starts in a stagnant mixture. Power is applied to the heating element using a DC power supply (typically with 10 A at 10 V), increasing its temperature from room temperature until ignition is observed. Once ignition has occurred, the energy input to the glow plug is negligible compared to the chemical energy release. The time to reach ignition varies with the size and resistivity of the element from 5 to 10 s. A thin wire K-type thermocouple is used to measure the temperature for all hot surfaces except the wire. The temperature of the glow plugs is measured at their hottest point (found on the side of the Autolite 1110 glow plug 1.7 mm from the top and on the side of the Bosch glow plug 2.5 mm from the top). The nominal response time of the thermocouple is 0.5 s. The pressure is monitored at

https://doi.org/10.1017/jfm.2013.495 Published online by Cambridge University Press

the top of the vessel with a dynamic pressure transducer ($\geqslant$10 kHz, Endevco Model 8530B-200).

In order to facilitate the comparison with the simulation results, a stagnation plate is fitted around the hot surface, which serves as the reference geometry. The diameter of the stagnation plate is 58 mm, slightly less than the diameter of the window. In addition, an array of seven K-type thermocouples, placed 1 cm apart from each other along the vertical axis above the glow plug, is used to characterize the plume created by the hot surface before ignition occurs. The comparison of the experimental results with the simulations results is presented later.

2.2. *Numerical simulations*

The governing equations of fluid motion for the simulations performed here are the variable density, low-Mach-number Navier–Stokes equations

$$\partial_t \rho + \boldsymbol{\nabla} \cdot (\rho \boldsymbol{u}) = 0, \tag{2.1}$$

$$\partial_t (\rho \boldsymbol{u}) + \boldsymbol{\nabla} \cdot (\rho \boldsymbol{u}\boldsymbol{u}) = -\boldsymbol{\nabla} p + \boldsymbol{\nabla} \cdot \boldsymbol{\tau} + \rho \boldsymbol{g}, \tag{2.2}$$

where $\boldsymbol{\tau}$ is the viscous shear stress tensor and $\boldsymbol{g}$ represents the gravity vector.

The simulations are performed using the NGA code (Desjardins *et al.* 2008) which uses high-order conservative finite difference schemes developed for the simulation of variable density turbulent flows. The finite difference scheme for velocity is second-order in time and space. A third-order upwind differencing scheme (QUICK) is used for transport of scalar variables such as the progress variable and unburned gas temperature (Leonard 1979). A lookup table procedure is used to determine species and mixture properties as a function of the reaction progress.

The numerical simulation only models the vessel above the stagnation surface, which is roughly in the middle of the experimental vessel (shown in figure 1) giving a volume of 2 l. The symmetry of the problem allows the reaction vessel to be modelled using a 2D axisymmetric mesh. The total number of mesh points is $N_x \times N_r = 984 \times 624$. The mesh is locally refined in the vicinity of the glow plug with 804 points corresponding to one height of the glow plug in the vertical direction above the base of the glow plug and 504 points corresponding to 1.5 diameters of the glow plug in the horizontal direction to the left and right from the centreline of the domain. A Dirichlet boundary condition is assigned to the glow plug surface. The temperature at any location on the glow plug is constant in time but it varies in space along the surface of the glow plug to match experimentally determined values.

2.2.1. *Chemistry tabulation*

The code relies on a modified flamelet progress variable (FPV) approach. The reader is referred to Menon, Boettcher & Blanquart (2013) for more details on the combustion modelling approach, and previous work on tabulated chemistry approaches by Peters (1988), Oijen & de Goey (2000), Pierce (2001) and Pierce & Moin (2004).

2.2.2. *Reaction mechanism*

The reaction mechanism used in this work is one for heavy hydrocarbon fuels which has been extensively validated over a wide range of temperatures, pressures, and equivalence ratios (Blanquart, Pepiot-Desjardins & Pitsch 2009; Narayanaswamy, Blanquart & Pitsch 2010). It is provided electronically as supplemental material available at http://dx.doi.org/10.1017/jfm.2013.495. *N*-heptane is used as the fuel in all simulations (in place of *n*-hexane) since the chemistry of *n*-heptane is better understood than that of *n*-hexane. This decision is justified by previous studies which have shown that normal alkanes show very similar ignition and flame propagation

https://doi.org/10.1017/jfm.2013.495 Published online by Cambridge University Press

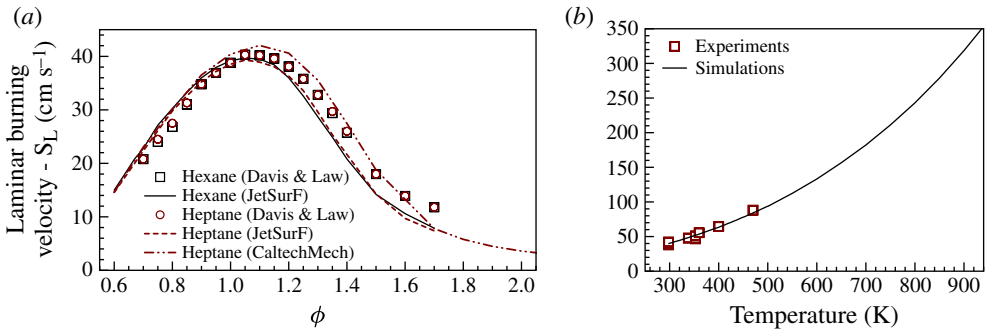


FIGURE 2. (Colour online) (*a*) Laminar burning velocity of *n*-heptane and *n*-hexane at room temperature and atmospheric pressure from experiments (Davis & Law 1998*a*) and simulations (CaltechMech results from Blanquart *et al.* (2009) and Narayanaswamy *et al.* (2010) and JetSurF results from Wang *et al.* (2010)). (*b*) Laminar burning velocity of stoichiometric *n*-heptane as a function of the initial gas temperature as found in experiments and predicted using the chemical reaction mechanism ($\phi = 1.0$), using experimental data from Davis & Law (1998*a*), Huang *et al.* (2004), Kumar *et al.* (2007), Ji *et al.* (2010), Kelley *et al.* (2011) and Van Lipzig *et al.* (2011).

characteristics (Davis & Law 1998*b*; Shen *et al.* 2009; Westbrook *et al.* 2009; Kelley *et al.* 2011).

To assess the accuracy of the chemistry representation, the detailed reaction mechanism is used to estimate flame speeds for *n*-heptane/air mixtures at different equivalence ratios and unburned gas temperatures at which experimental data are available from the literature (Davis & Law 1998*a*; Huang, Sung & Eng 2004; Kumar *et al.* 2007; Ji *et al.* 2010; Kelley *et al.* 2011; Van Lipzig *et al.* 2011). The agreement between experiments and simulations is excellent for lean and stoichiometric mixtures as shown in figure 2(*a*). Under rich conditions, the measured flame speeds exhibit more scatter.

Predicting the variation of the laminar flame speeds on the background temperature is especially important for the present work as the temperature inside the plume ranges from 300 to 900 K. For the experimental measurements, a temperature increase of just 100 K can raise the laminar flame speed by over 50 %. Although experimental data are not available at the highest temperatures observed in the plume, the solution using detailed chemistry and transport predicts that the flame speeds could be as high as 200–300 cm s^{-1} immediately above the glow plug (figure 2*b*).

2.3. *Initial thermal plume*

A direct effect of heating the hot glow plug is to develop a thermal plume due to the diffusion of heat from the hot surface into the cold unburned gas mixture. The accompanying change in density results in a buoyancy-induced accelerating flow towards the top surface of the chamber. This upward flow establishes a density, velocity, and temperature gradient in the combustion chamber prior to the ignition event. As will be seen in the following section, this initial stratification (horizontal and vertical) influences the overall behaviour of the flame front. The extended heating and induced fluid motion is expected to increase the temperature required for ignition above that of an instantaneously heated surface. However, specific experiments to confirm this were not part of the investigation. It is important to note that at the

https://doi.org/10.1017/jfm.2013.495 Published online by Cambridge University Press

current temperature ramp rate the time for the flow field to adjust is much smaller than the time to increase the glow plug temperature.

To reproduce the sequence of events as observed in the experiment, the present simulations are carried out in two steps: first a non-reacting simulation until steady state; then a reacting simulation. The non-reacting simulation is carried out by specifying the same temperature profile on the glow plug surface as measured in the experiments applied to the glow plug surface. In the absence of chemical reactions, diffusion of heat produces a natural convection of hot gases resulting in the development of a thermal plume. This configuration is simulated until a steady-state solution is reached while the reaction progress variable remains at zero. The temperature is observed to decrease with height above the glow plug, as anticipated from laminar plume theory in reasonable agreement with $\Delta T \sim x^{-3/5}$ (Boettcher 2012).

Measurements of the actual flame temperature are not possible in the current configurations and are best accomplished in a steady-state burner with a coated platinum–rhodium thermocouple (Kint 1970; Tran, Glaude & Battin-Leclerc 2013). For a freely propagating flame, the response time, temperature range, conduction within and radiation losses from the thermocouple would introduce large errors into the measurement for this configuration.

3. Flame propagation regimes

In the experiments, ignition has typically been observed to occur at the top surface of the glow plug (Boettcher 2012). Based on this observation, ignition is simulated in the computations by introducing a small pocket of burned gases close to the top of the glow plug and at a temperature around 920 K. This results in a positive value for the progress variable source term and the formation of a flame front. These reacting simulations are initiated from the steady-state, non-reacting simulations presented in the previous section.

The flame propagation is investigated as a function of various parameters including the initial pressure, and the mixture composition. Several different flame behaviours are observed in the experiments and simulations as the mixture composition is varied. In this section, the focus is on presenting these different regimes and the effect of mixture composition on the flame behaviour through its influence on the flame propagation speed.

3.1. *Single flame*

A single flame is observed for equivalence ratios ranging from the lean flammability limit ($\phi = 0.56$, Zabetakis 1965) to fuel-rich mixtures with twice the amount of fuel present than necessary for complete combustion ($\phi = 2.0$). Figure 3 shows frames from the high-speed schlieren video for a case with an equivalence ratio of $\phi = 1.20$. In the images, the circular outline of the window is visible as well as the horizontal edge of the stagnation plate at the bottom. The glow plug is centred at the bottom of the image and its temperature is measured at its hottest point with the thermocouple visible in its holder on the right-hand side. Figure 4 shows simulation results for a fuel-rich *n*-heptane/air mixture with the same equivalence ratio, $\phi = 1.2$. The images show density contours in the simulation domain, ranging linearly from the unburned density ($\sim$1 kg m^{-3}, blue) to the burned density ($\sim$0.1 kg m^{-3}, red). The black line is an isocontour of progress variable equal to 0.15 and represents the flame front location. This same representation of the flame front location is used in all simulation results.

https://doi.org/10.1017/jfm.2013.495 Published online by Cambridge University Press

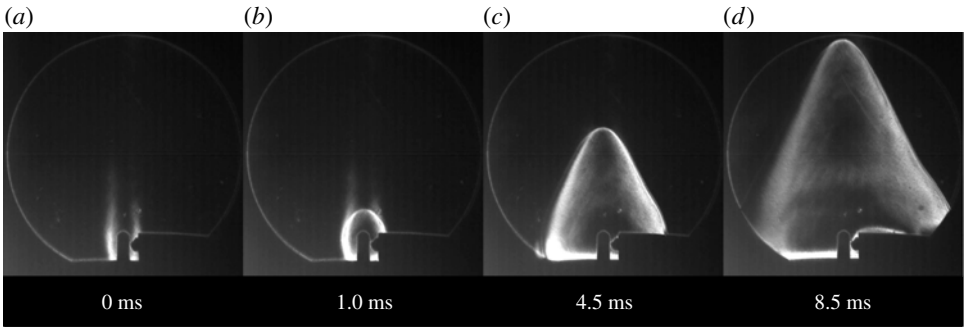


FIGURE 3. Dark background schlieren visualization of the flame propagation for a hexane/air mixture (Bosch glow plug, $\phi = 1.2$).

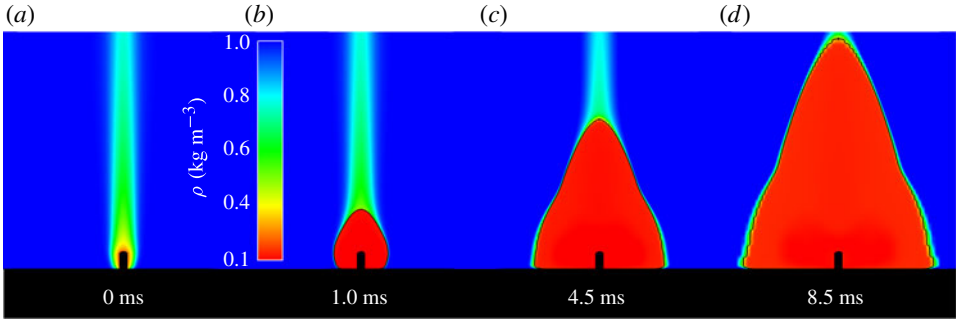


FIGURE 4. (Colour online) Simulation results for flame propagation phenomena (Bosch glow plug, $\phi = 1.2$).

In both the experimental and simulation sequences, the first frame shows the plume resulting from heating by the glow plug prior to ignition. Once ignition occurs, an approximately ellipsoidal flame develops. As discussed in the previous section, the gas temperature has a strong influence on the flame propagation speed due to the strong dependence of the reaction rate on temperature. At early times, the bulk of flame remains inside the hot plume and propagates vertically and horizontally at similar speeds (figures 3*b* and 4*b*). When the bulk of the flame extends beyond the hot plume, it enters a region of lower unburnt temperature on the sides, and slows down due to the temperature drop. From that point on, the flame propagates faster at the top giving it the conical or pear-like shape. The flame continues to grow until the whole mixture in the combustion chamber is burnt.

From measurements of the horizontal and vertical propagation of the flame it has been determined that the horizontal flame propagation speed, V_f, is approximately equal to that of a planar flame, i.e. the product of the expansion ration, ϵ, and the laminar flame speed relative to the unburned gas, S_L, (Boettcher 2012; Menon *et al.* 2013).

3.2. *Puffing flames*

The usual combustion mode following ignition in a closed vessel is a single quasi-spherical flame that spreads in all directions. The flame may eventually be distorted by buoyancy at low propagation velocities for very lean or rich mixtures (Bane *et al.* 2011) and also by the flow resulting from the shape of the enclosure or instabilities

https://doi.org/10.1017/jfm.2013.495 Published online by Cambridge University Press

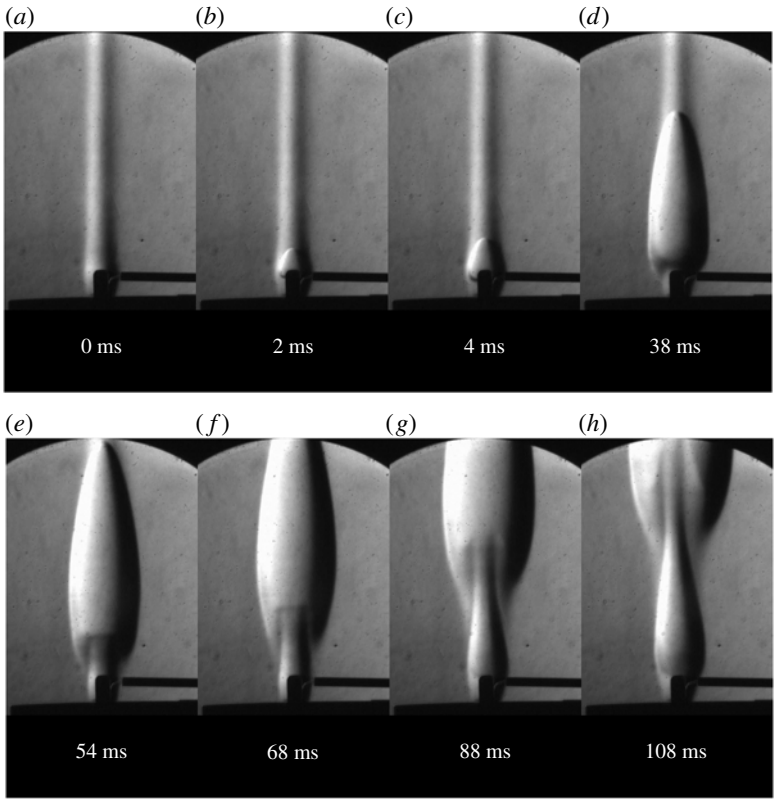


FIGURE 5. Schlieren images of ignition and subsequent flame propagation of one puff and the beginning of a second puff in a mixture of *n*-hexane in air at atmospheric pressure ($\phi = 3.0$). The hot surface is an Autolite 1110 glow plug in a 60 mm diameter aluminium cylinder in a closed 22 l combustion vessel.

of various types (Palm-Leis & Strehlow 1969; Sivashinsky 2002). In the present case, the hot surface establishes a thermal buoyant plume in the vessel, which induces an initial upward flow prior to ignition. This thermal plume is shown in the first schlieren image in figure 5(*a*) for a rich *n*-hexane/air mixture ($\phi = 3.0$). Schlieren images were also taken in inert mixtures, and under those conditions a steady plume without any oscillatory behaviour was observed.

The thermal plume is also visible in the simulation in figure 6(*a*). Next, the mixture ignites near the tip of the glow plug and a flame propagates quickly upward along the thermal plume. At this high equivalence ratio, the laminar burning velocity is very low at room temperature, as found outside the hot plume. On the other hand, the flame speed is significantly enhanced inside the hot plume. The combination of the temperature differential (between inside and outside the plume) and the buoyancy-induced flow gives the flame its very elongated shape. In addition, in the schlieren images, it can also be observed that the flame does not propagate downward after ignition due to the upward flow velocity at the glow plug base.

Once ignition has occurred, the temperature in the region above the hot surface is determined by combustion products and is greater than the temperature in the initial hot plume. The upward motion of the buoyant hot products entrains cold premixed but unreacted gases. This enhanced entrainment velocity also limits the

https://doi.org/10.1017/jfm.2013.495 Published online by Cambridge University Press

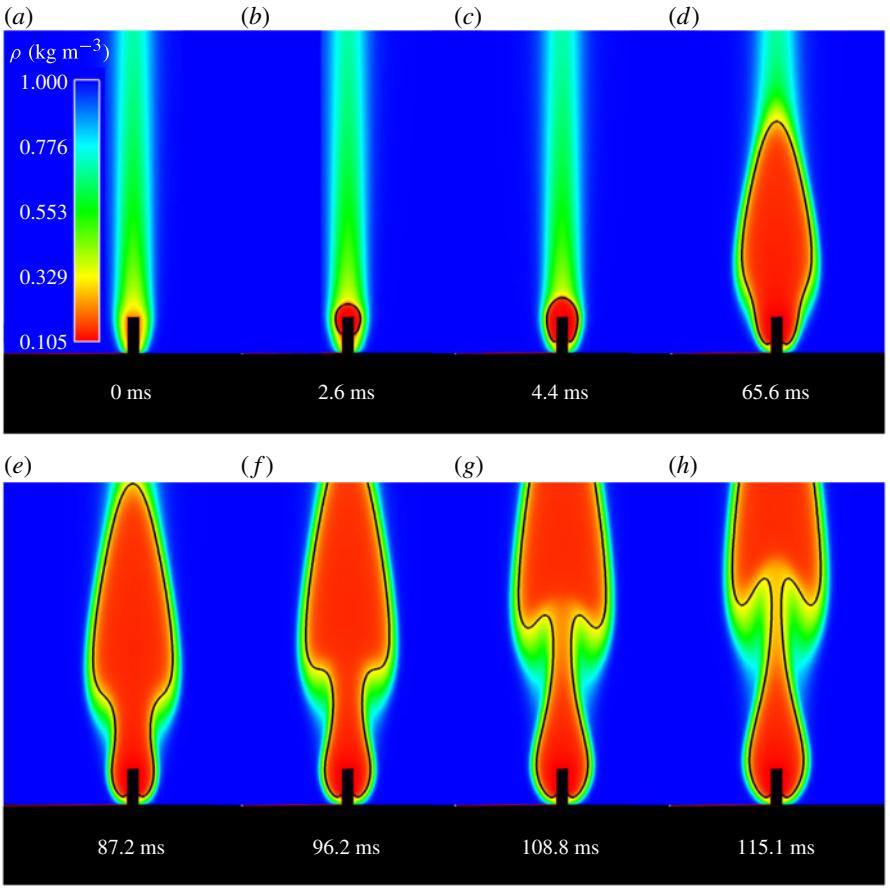


FIGURE 6. (Colour online) Simulation results for flame propagation phenomena at an equivalence ratio of $\phi = 2.5$. The black line represents the location of the flame front as marked by the isocontour of the progress variable, $C = 0.15$.

horizontal spreading of the flame. The resulting behaviour is a continuous but periodically varying cylindrical flame extending upward from the thermal ignition source, characterized by a sequence of individual flame 'puffs'. The 'puffing' flame that develops following an initial ignition transient determines the temperature distribution and flow field behaviour. The puffing behaviour appears to be a result of the instability of the flow and the flame sheet due to the interaction between the entrainment, buoyancy-induced flow, and flame dynamics.

This puffing behaviour is also captured in the simulations, whose detailed results will be used later. Figure 6 shows a sequence of images for a mixture equivalence ratio of $\phi = 2.5$ (*n*-heptane/air) obtained from the simulations. The simulation results are plotted using contours of constant density with the black line showing the location of the flame front. As in the experiments, the flame remains anchored at the glow plug accompanied by a periodic generation of flame 'puffs'. The critical equivalence ratio at which puffing is first observed in simulations is ~2.5. The laminar flame speed at this mixture ratio is 1.65 cm s^{-1}. In the experiments, the onset of puffing occurs at equivalence ratios between 2.7 and 3.0, consistent with simulation results given the experimental uncertainty in mixture composition (Boettcher 2012; Menon *et al.* 2013).

https://doi.org/10.1017/jfm.2013.495 Published online by Cambridge University Press

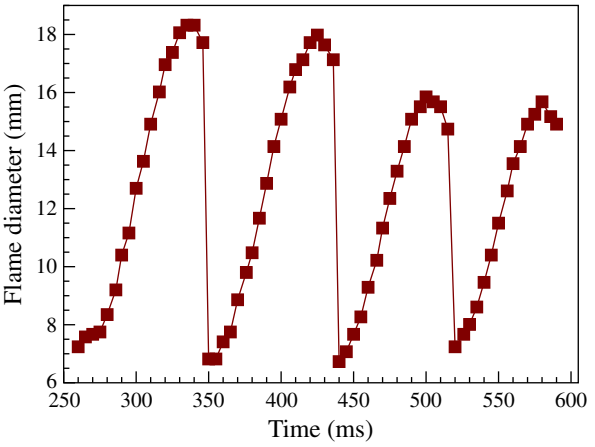


FIGURE 7. (Colour online) Flame diameter as a function of time 5 mm above the glow plug (experimental result at $\phi = 3.0$). The interval between between puffing cycles is 80 ms $\pm$ 10 ms.

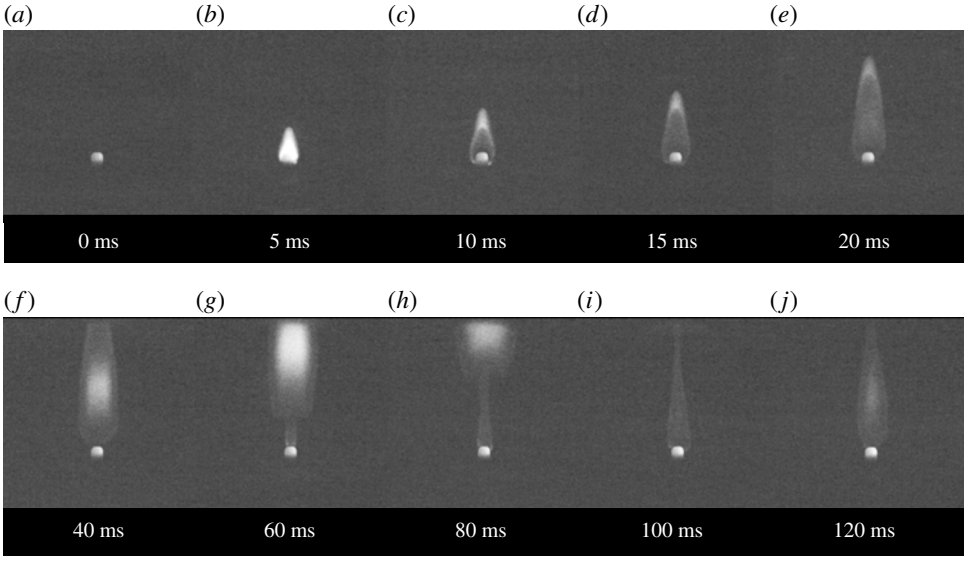


FIGURE 8. Direct imaging of CH^* molecules through a bandpass filter ($\phi = 3.0$).

The periodicity of the phenomenon can be captured by measuring the flame diameter at a fixed location above the glow plug. The results from an experiment at an equivalence ratio of $\phi = 3.0$ are shown in figure 7. The flame initially expands outward until the 'puff' thus formed gets convected upward and the cyclic phenomena continue with the flame expanding again at the top of the glow plug.

A sequence of images showing the CH^* luminescence in figure 8 further illustrates the puffing phenomenon. Figure 8(*a*) shows the hot tip of the glow plug where ignition occurs. Then, in the following frames, the flame propagates outward and more quickly in the hot plume above the glow plug. The puffing process occurs at a frequency of ~6–15 Hz depending on the initial composition. The bright region inside the flame above the glow plug is not due to CH^* emission. It is due to the broadband, black-

https://doi.org/10.1017/jfm.2013.495 Published online by Cambridge University Press

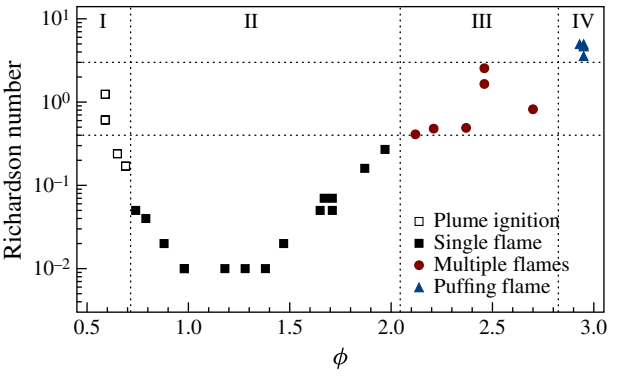


FIGURE 9. (Colour online) Ignition behaviour as function of Richardson number for varying equivalence ratio at atmospheric pressure in the 2 l combustion vessel.

body radiation coming from the soot particles. A premixed hydrocarbon-based flame at such a rich equivalence ratio is expected to yield significant soot levels. The puffing frequency scaling and the physics of the puffing are presented in more detail in the following sections.

3.3. *Richardson number and combustion modes*

In the present experiments, the different modes of combustion can be attributed to a shifting balance between flame propagation speed and buoyancy of the burned gases. The buoyancy effect depends on the densities of the burned and unburned gases and the gravitational acceleration. This suggests that the different regimes can be characterized by the Richardson number, *Ri*, which represents the ratio of buoyancy to inertial effects in gas motion,

$$Ri = \left(\frac{\rho_u - \rho_b}{\rho_u + \rho_b}\right)\frac{gL}{V_f^2}, \tag{3.1}$$

where ρ_u and ρ_b are the unburned and burned gas densities respectively, g is the gravitational acceleration, L is the height of the glow plug, and V_f is the measured horizontal flame propagation velocity. The burned density, ρ_b, is calculated from a constant pressure equilibration of the chemical system. The various flow regimes are shown in figure 9 together with the variation of the Richardson number (evaluated from the experiments) with the mixture composition. The Richardson number varies by a factor of 100 over the range of equivalence ratio examined in this study. This is primarily due to the dependence of flame speed on equivalence ratio shown in figure 2(*b*). The ratio ρ_u/ρ_b varies modestly, between 5.5 and 8, for the range of composition presented in figure 9. As shown, the combustion behaviour can be divided into four regions as a function of the equivalence ratio.

Region I. Near the lean flammability limit, we observe an ignition and flame propagation phenomenon that is different from the one presented in figure 3. For such lean mixtures, the minimum ignition temperature is raised to above 1170 K, which leads to an increase in the size of the plume. Ignition is not observed to occur in a small kernel, but over a wider area within the plume. After ignition, the flames propagate quickly in the hot plume and consume the entire volume. This phenomenon is observed in mixtures ranging from $\phi = 0.59$ to 0.69.

https://doi.org/10.1017/jfm.2013.495 Published online by Cambridge University Press

Region II. For a Richardson number less than 0.4, a single flame is observed with the exception of the two lowest equivalence ratios (region I). In region II the Richardson number is small, suggesting that the buoyancy-induced flow is negligible when compared to the flame propagation speed. In that case, the flame takes a triangular shape and consumes the whole mixture in a single combustion event.

Region III. For Richardson numbers between 0.4 and 3, the initial flame kernel grows and is lifted simultaneously by buoyancy forces. The mixture ignites again in the wake of the first flame and a second flame kernel is generated. The absence of a continuous flame at the top of the glow plug was further verified using CH^* imaging.

Region IV. For Richardson numbers above 3, puffing flames are observed. At these large Richardson numbers, buoyancy is much stronger than inertia: the flame propagates slowly in the horizontal direction and it is rapidly lifted by buoyancy. Careful inspection of the CH^* pictures indicate that a continuous flame is anchored at the tip of the glow plug.

This analysis of the combustion modes as a function of the Richardson number suggests that when buoyancy and inertia are of the same magnitude, flame re-ignition is observed (region III). A further decrease in the inertia leads to puffing flames in region IV.

4. Puffing frequency

In the previous section, the puffing phenomenon was found to depend on the composition of the mixture. Other factors such as the size of the hot surface or vessel volume might also affect this phenomenon. The effect of the vessel volume is also of special interest, because for very small vessel sizes the combustion products could force the flow into a large-scale recirculation or result in coupling of acoustic modes with flame motion. The following section provides details of the effects of these parameters and gives dimensional arguments on how the frequency changes as a function of the flame propagation speed and gravity.

4.1. *Glow plug size and vessel size*

The experiments were performed with the three different heat sources listed in table 1. The measurements show that there is very limited dependence of the puffing frequency on the igniter size (despite changes by almost two orders of magnitude), as well as heating power input.

The volume of the vessel may contribute to the puffing phenomenon via two distinct behaviours: first, flame acoustic coupling; second, creation of a large-scale recirculation zone. To test the role of the vessel volume, we changed the volume by a factor of 10 in the experiments. The puffing frequency did not change noticeably. A similar analysis was performed with numerical simulations by changing the size of the modelled glow plug by a factor of 0.5 and 2 and the size of the vessel from 1 to 5 l. The large vessel is only modelled to a size of 5 l to limit the number of grid points and the computational time required. The puffing frequency was not found to change noticeably. It is important to note, however, that the numerical simulations cannot capture flame acoustic coupling and can only test for the presence of a large-scale recirculation zone. The combination of experimental and numerical observations indicates that the frequency is a function of the flame dynamics and the flow induced by the flame, and is independent of the igniter and vessel volume. This rules out the possibility that the periodic motion is caused by a recirculation created by the flame pushing the unburned gases upward, stagnating at the top, and pushing fluid down the

https://doi.org/10.1017/jfm.2013.495 Published online by Cambridge University Press

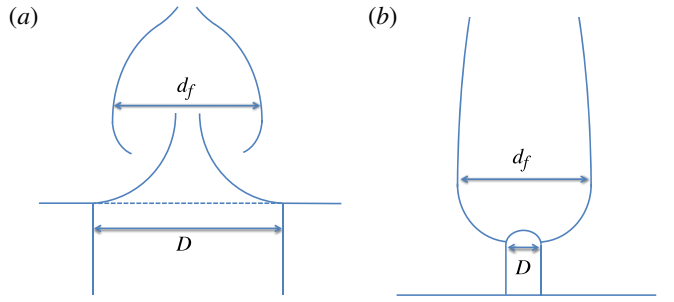


FIGURE 10. (Colour online) (*a*) Flame diameter d_f and pool diameter D, based on Cetegen & Ahmed (1993). (*b*) Flame diameter d_f and hot surface D, for premixed puffing flames.

side and back into the flame. The independence of frequency from vessel size also rules out acoustic interactions with the enclosure as a possible puffing mechanism.

4.2. *Scaling laws*

The observed frequency is a function of the buoyancy-induced flow, with no puffing being observed in zero-gravity conditions, making gravity, g, one of the parameters of interest. The same simulation that gave the results shown in figure 6 was re-run without gravity and no puffing phenomena was observed. Two scaling laws (dimensional analysis) for buoyant flows are of relevance to the present analysis. They are presented below.

4.2.1. *Cetegen & Ahmed (1993)*

Buoyant plumes and pool fires have instabilities and periodic motions that are very similar to those observed in the present premixed puffing flames. As a first approximation, the frequency behaviour of plumes and pool fires can be estimated using dimensional analysis.

The main length scale is the diameter of the burner, D, through which either a buoyant plume of light gas, such as helium, combustion products from a preburner, or a pool of evaporating fuel is introduced. Cetegen & Ahmed (1993) suggest that the non-dimensional ratio

$$\frac{f^2 D}{g} \tag{4.1}$$

has a universal value. This implies that at a constant gravitational acceleration,

$$f \sim D^{-1/2}. \tag{4.2}$$

Cetegen & Ahmed (1993) compiled data for many different gaseous and liquid fuels as well as light gases, and showed good agreement using this scaling argument for burner sizes of approximately 10^{-2} to 10^{1} m.

For pool fires, the size of the pool determines the size of the flame. The fuel from the liquid or gaseous pool has to mix with the air outside to create a combustible mixture. This mixing interface originates near the edge of the fuel pool. The diameter of the flame, d_f, is therefore fixed and proportional to the pool diameter as shown in figure 10.

$$d_f \propto D. \tag{4.3}$$

https://doi.org/10.1017/jfm.2013.495 Published online by Cambridge University Press

The puffing flames described here, however, are premixed flames. The diameter of the flame significantly exceeds that of the hot surface since the flame starts at the hot surface and propagates outward until the flame front becomes unstable and the upward flow sweeps it away. The flame initially propagates outward quasi-spherically so that the radius scales as $\epsilon S_L t$, where ϵ is the density ratio across the flame front and S_L is the laminar flame speed relative to the unburned gas. The flame diameter increases until the instability takes over, giving the time scale of $T \sim 1/f$. We propose that the characteristic diameter of the flame can be modelled as the sum of the two terms,

$$d_f = 2\frac{\epsilon S_L}{f} + D. \tag{4.4}$$

The first term represents the diameter of the flame at the peak of the puffing cycle and the second term represents the diameter of the hot surface, D, the initial position from which the flame starts.

In the present experimental study, hot surfaces with different diameters were considered, ranging from $D = 0.1$ mm to $D = 5$ mm. The puffing period, T, is $\sim$0.1 s for flame propagation speeds of $\sim$0.2 m s^{-1}. Under these conditions, the flame diameter changes by only 12.5 % for a change in hot surface size of almost two orders of magnitude. As an initial approximation, if the diameter of the hot surface is neglected, a new non-dimensional ratio can be formulated similar to the one proposed by Cetegen & Ahmed (1993) in (4.1),

$$N_B = \frac{f\epsilon S_L}{g} = \frac{\epsilon S_L}{gT}, \tag{4.5}$$

and has a value of 0.2–0.3, which is comparable to 0.23 found by Cetegen & Ahmed (1993). Cetegen & Ahmed (1993) give the scaling for pool fires at normal gravity as $f = 1.5D^{-1/2}$. Squaring both sides and dividing through by g gives $(f^2 D)/g = 0.23$.

These results lead to the following scaling for a fixed ϵS_L,

$$f \propto g, \tag{4.6}$$

and for a fixed g,

$$f \propto (\epsilon S_L)^{-1} \quad \text{or} \quad T \propto (\epsilon S_L)\,. \tag{4.7}$$

These scaling results are compared with experimental data in the subsequent sections.

4.2.2. *Durox, Yuan & Villermaux (1997)*

Durox *et al.* (1997) investigated the flickering of jet diffusion flames and arrived at a different set of scaling relations. Tests were performed at varying pressure and at varying gravitational acceleration, which was achieved during parabolic flight tests. In these experiments, the mean diameter of the flame is greater than the nozzle diameter. In contrast, for pool fire experiments, the mean flame diameter is generally smaller than the pool diameter. From dimensional analysis the frequency, f, is scaled with the gravitational acceleration, g, and the kinematic viscosity, ν,

$$f^3 \sim \frac{g^2}{\nu}. \tag{4.8}$$

Durox *et al.* (1997) performed a detailed theoretical analysis of the flame instability, where the flame creates a constant inflow of hot gases forming a shear layer across the flame front. Durox *et al.* argued that the most amplified frequencies, f, in this flow are

https://doi.org/10.1017/jfm.2013.495 Published online by Cambridge University Press

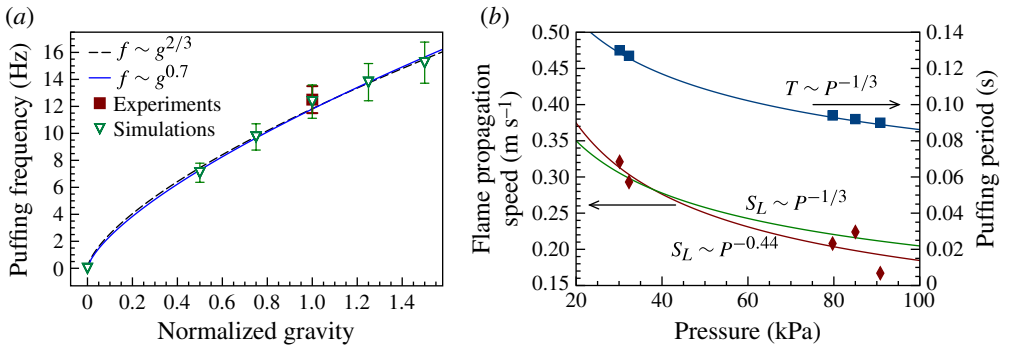


FIGURE 11. (Colour online) (*a*) Simulation results for the puffing frequency as a function of gravitational acceleration. (*b*) Experimental results for puffing frequency and flame propagation speed as function of initial pressure at $\phi = 2.5$.

given by

$$f = c\left[\left(\frac{\rho_u - \rho_b}{\rho_b}\right)^2 \frac{g^2}{\nu_b}\right]^{1/3}, \tag{4.9}$$

where c is a constant, ρ_u and ρ_b are the unburned and burned density, g is the gravitational acceleration, and ν_b is the viscosity of the burned gas. This scaling is based on the developments of the instabilities at a certain height above the nozzle exit, but can also be obtained by dimensional analysis when considering only the effects of buoyancy acceleration (m s^{-2}) and kinematic viscosity (m^2 s^{-1}). Note that this model predicts that the frequency is dependent on viscosity rather than burning speed because the mode of combustion is non-premixed.

4.3. *Effect of gravity*

Gravity creates a buoyancy force on the burned gases, which are less dense than the surrounding gases, and lifts the flame upward once it has reached a critical size. Simulation results shown in figure 11(*a*) exhibit a nonlinear behaviour ($f \sim g^{0.7}$), and confirm that the frequency of the puffing changes with the magnitude of gravitational acceleration. This is consistent with the flame puff being lifted by the acceleration of gravity and the hydrostatic pressure, creating an entrainment flow pinching the flame together. Both of these effects are increased as the acceleration due to gravity is increased. On the other hand, as acceleration due to gravity is reduced, the frequency decreases to the point where in the absence of gravity, no puffs are generated, and the puffing frequency goes to zero (infinite puffing period).

Figure 11(*a*) also shows the scaling ($f \sim g^{2/3}$) derived by Durox *et al.* (1997) for the puffing frequency as a function of gravitational acceleration. The nonlinear behaviour obtained from the simulation results is captured well by this scaling law. The linear scaling proposed by Cetegen & Ahmed (1993) in (4.6) is not as consistent with the numerical simulations. The deviation from a linear relationship might be explained as a result of the initial hot surface diameter (D) neglected in (4.4).

4.4. *Effect of pressure*

In an attempt to differentiate between the two proposed scaling laws, we performed additional experiments by varying the initial pressure from 25 to 100 kPa for

https://doi.org/10.1017/jfm.2013.495 Published online by Cambridge University Press

a $\phi = 2.5$ *n*-hexane/air mixture. The results shown in figure 11(*b*) indicate that an increase in pressure leads to an increase in the puffing frequency. The observed experimental dependence is close to

$$f \sim P^{1/3} \quad \text{or} \quad T \sim P^{-1/3}. \tag{4.10}$$

From a theoretical point of view, the background pressure (P) has an effect on both the kinematic viscosity of the burned gases and the flame propagation speed:

$$\nu_b \sim 1/P \quad \text{and} \quad S_L \sim P^{-0.44}. \tag{4.11}$$

The pressure dependence of the flame speed was estimated from the experimental data shown in figure 11(*b*). Also shown in figure 11(*b*) is the scaling law $S_L \sim P^{-1/3}$ that yields the exact comparison between Cetegen & Ahmed's 1993 scaling in (4.7) and (4.10). The resulting scaling relationships following the analyses of Durox *et al.* (1997) and Cetegen & Ahmed (1993) are respectively

$$T \sim P^{-1/3} \quad \text{and} \quad T \sim P^{-0.43}. \tag{4.12}$$

Both analyses produce very similar scaling laws that are consistent with the experimental observations.

To resolve these effects independently, additional simulations were performed to identify the change in puffing frequency solely due to the effect of viscosity. Changing viscosity while keeping the flame speed constant was found to have a negligible effect on the puffing frequency. Increasing or decreasing the viscosity by a factor of 10 from its normal value gave a $\pm 8\,\%$ change in puffing frequency. On the other hand, if viscosity were as important as shown by Durox *et al.* (1997) in (4.9), changing the viscosity by a factor of 10 would change the frequency by a factor of 2.2. Further, puffing behaviour was also observed for a simulation performed with no viscosity. This suggests that the effects observed in the experimental results in figure 11(*b*) are primarily due to the changes in flame propagation speed caused by changes in pressure.

In figure 12, the puffing period, $T = 1/f$, is plotted versus the flame propagation speed for both experiments and simulations. The experimental mixtures shown are *n*-hexane in air from $\phi = 2.15$–3.0 and at initial pressures varying from 25 to 100 kPa, 7 and 8 % hydrogen in air, as well as lean and rich hexane mixtures doped with hydrogen (see the following section). In agreement with the previously proposed scaling relationship (based on the scaling of Cetegen & Ahmed 1993), the puffing period increases approximately linearly with flame speed for all experimental and computational results. The deviation from a linear relationship can be rationalized as being due to neglecting the initial hot surface diameter (D) in (4.4). A more general expression may be derived by using the full form of (4.4).

The dependence of the puffing frequency on the flame propagation speed is not predicted by the scaling of Durox *et al.* (1997), which further justifies that flame propagation and buoyancy, rather than viscosity, control the instability mechanism.

4.5. *Overall scaling of the puffing period*

Following the arguments from Cetegen & Ahmed (1993), and assuming that the important length scale is the diameter of the hot products, we propose that the following expression must be a constant:

$$\frac{f^2 d_f}{g} = \frac{2\epsilon S_L f}{g} + \frac{f^2 D}{g} = C. \tag{4.13}$$

https://doi.org/10.1017/jfm.2013.495 Published online by Cambridge University Press

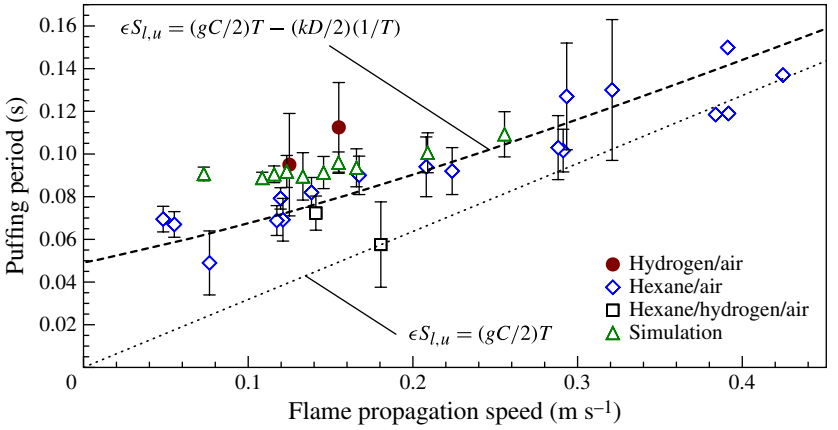


FIGURE 12. (Colour online) Puffing period versus horizontal flame propagation speed for *n*-hexane/air mixtures from $\phi = 2.15$–3.0, 7 % and 8 % hydrogen in air and hexane/hydrogen/air mixtures at atmospheric pressure. The error bars show $\pm\sigma$ uncertainty in the measured puffing period. Data points without error bars have an insufficient number of cycles to compute a variation. The composition for each of the data points is given in table 2.

We can rearrange this equation to give

$$\epsilon S_L = \frac{gC}{2}T - \frac{kD}{2}\frac{1}{T}, \tag{4.14}$$

where the flame propagation speed is a function of the puffing period as plotted in figure 12. This equation can be written as a quadratic equation for the puffing period,

$$\frac{gC}{2}T^2 - \epsilon S_L T - \frac{kD}{2} = 0. \tag{4.15}$$

An additional constant k has been introduced to provide a better fit to the experimental data and account for the fact that the initial flame diameter may not be exactly D. Using all experimental and numerical results, the coefficients C and k were found using a least-squares minimization ($C = 0.64$ and $k = 3.35$). Figure 12 shows both the experimental data and simulation results. The linear relation ($k = 0$) is also shown. While both are in general agreement with the observations, the nonlinear correlation (4.14) has a lower mean error in the puffing period (0.013 s) than the linear correlation (0.13 s).

A direct comparison with the scaling proposed by Cetegen & Ahmed (1993) is also possible by setting the flame speed to zero. In dimensional form, the frequency in Hz as a function of diameter in meters at 1 g is given by Cetegen & Ahmed (1993) as

$$f = 1.5\, D^{-1/2}. \tag{4.16}$$

Setting $S_L = 0$ in (4.14) leads to the following expression:

$$f = \sqrt{\frac{gC}{k}} D^{-1/2}. \tag{4.17}$$

Using the results obtained for the coefficients C and k, the constant of proportionality is $\sqrt{gC/k} = 1.4$ Hz m$^{1/2}$, which is within 10 % of the Cetegen & Ahmed value.

https://doi.org/10.1017/jfm.2013.495 Published online by Cambridge University Press

Exp./Sim.	Mixture	ϕ	V_f (m s^{-1})	T (s)	f (Hz)
Exp.	C_6H_{14} in air	3.00	0.048	0.070	14
Exp.	C_6H_{14} in air	3.00	0.055	0.067	15
Exp.	C_6H_{14} in air	3.01	0.076	0.049	20
Exp.	C_6H_{14} in air	2.98	0.12	0.069	14
Exp.	C_6H_{14} in air	3.00	0.12	0.079	13
Exp.	C_6H_{14} in air	3.00	0.12	0.069	14
Exp.	C_6H_{14} in air	3.00	0.14	0.082	12
Exp.	C_6H_{14} in air	2.50	0.17	0.090	11
Exp.	C_6H_{14} in air	2.50	0.21	0.094	11
Exp.	C_6H_{14} in air	2.50	0.22	0.092	11
Exp.	C_6H_{14} in air	2.49	0.29	0.10	10
Exp.	C_6H_{14} in air	2.75	0.29	0.10	10
Exp.	C_6H_{14} in air	2.50	0.29	0.13	7.7
Exp.	C_6H_{14} in air	2.54	0.32	0.13	7.7
Exp.	C_6H_{14} in air	2.41	0.38	0.12	8.3
Exp.	C_6H_{14} in air	2.15	0.39	0.15	6.7
Exp.	C_6H_{14} in air	2.25	0.39	0.12	8.3
Exp.	C_6H_{14} in air	2.15	0.43	0.14	7.1
Exp.	H_2 in air	0.18	0.13	0.10	11
Exp.	H_2 in air	0.21	0.16	0.11	9.1
Exp.	5.9 % C_6H_{14} + 5.0 % H_2 in air	—	0.14	0.072	14
Exp.	1.1 % C_6H_{14} + 1.0 % H_2 in air	—	0.18	0.058	17
Sim.	C_7H_{16} in air	3.0	0.073	0.091	11
Sim.	C_7H_{16} in air	2.8	0.12	0.091	11
Sim.	C_7H_{16} in air	2.7	0.12	0.092	11
Sim.	C_7H_{16} in air	2.6	0.13	0.090	11
Sim.	C_7H_{16} in air	2.5	0.15	0.091	11
Sim.	C_7H_{16} in air	2.4	0.16	0.096	10
Sim.	C_7H_{16} in air	2.3	0.17	0.094	11
Sim.	C_7H_{16} in air	2.2	0.21	0.10	10
Sim.	C_7H_{16} in air	2.1	0.26	0.11	9.1

TABLE 2. Experimental and simulated mixtures with their corresponding equivalence ratio (ϕ) and their corresponding flame propagation speeds, puffing periods, and puffing frequencies from figure 12.

5. Physics of puffing

Experiments and simulations have both demonstrated a periodic motion associated with flame propagation in rich premixed hydrocarbon/air mixtures (and lean hydrogen flames). We have also verified that the frequency of this periodic motion is linked to the flame propagation speed and acceleration due to gravity. In order to get more insight into the puffing mechanism, the simulation results are used to analyse the instantaneous flow field.

5.1. *Flow field analysis*

The overall flow field is created by three different effects, all of them resulting from the combustion process. First, across the flame, the temperature increases, which lowers the density. This volumetric expansion across the flame induces a *dilatation* flow ahead of the flame because the flow is subsonic. Second, the lighter gases on the burnt side of the flame are accelerated upward by *buoyancy*, creating an entrainment flow at the bottom of the flame. Finally, at the flame front, *vorticity* is created, predominantly from baroclinic torque arising from the misalignment of the density

https://doi.org/10.1017/jfm.2013.495 Published online by Cambridge University Press

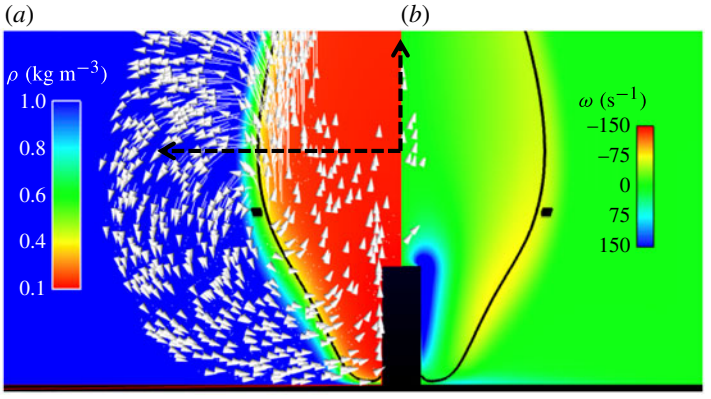


FIGURE 13. Flow field at 150 ms. Contours of density (*a*) and out-of-plane vorticity (*b*). The black line corresponds to an isocontour of the progress variable at $C = 0.15$. The dashed arrows show the x and y coordinate locations used in figure 14.

gradient across the flame and the hydrostatic pressure gradient. The inflow created by the combination of these three effects (dilatation, buoyancy, and vorticity) opposes the flame propagation at the bottom of the flame. The contribution due to each individual effect is investigated in detail in the following sections.

5.1.1. *Buoyancy*

The simulation results provide the instantaneous velocity vectors as shown in figure 13 for an *n*-heptane/air mixture at $\phi = 2.5$. In the laboratory frame, the flow outside the flame appears to rotate about a point (shaded in black) that translates as the puffing cycle progresses. The location of the centre of apparent rotation is identified using a technique similar to those of Graftieaux, Michard & Grosjean (2001) and Wyzgolik & Baillot (2008). The fluid particles, however, do not rotate around this point. A more detailed analysis of the flow field shows that the trajectory of the fluid elements outside the flame is more complex due to the competing effects of displacement and entrainment.

Buoyancy accelerates the burned gases upward. If we estimate the resulting velocity, U, starting from zero and after one puffing cycle ($T = 0.1$ s), we obtain

$$U \sim AtgT, \tag{5.1}$$

where At is the Atwood number, $At = (\rho_u - \rho_b)/(\rho_u + \rho_b)$. This buoyancy-induced velocity is of the same order of magnitude as the velocities observed at the centreline of the domain shown in figure 14. As the plume of hot gases is lifted by buoyancy, it pushes the cold gases situated above the flame and entrains the cold gases located below the flame. This creates an apparent rotation, while the flow is mostly irrotational.

5.1.2. *Vorticity*

A second potential source of rotation is due to vorticity production at the flame front. To estimate the flow induced by vorticity, we first consider the vorticity equation obtained by taking the curl of the Navier–Stokes equation:

$$\frac{\partial \boldsymbol{\omega}}{\partial t} + (\boldsymbol{u} \cdot \nabla)\,\boldsymbol{\omega} = (\boldsymbol{\omega} \cdot \nabla)\,\boldsymbol{u} - \boldsymbol{\omega}\,(\nabla \cdot \boldsymbol{u}) + \frac{1}{\rho^2}\,[\nabla\rho \times \nabla p] + \nu\nabla^2\boldsymbol{\omega}. \tag{5.2}$$

https://doi.org/10.1017/jfm.2013.495 Published online by Cambridge University Press

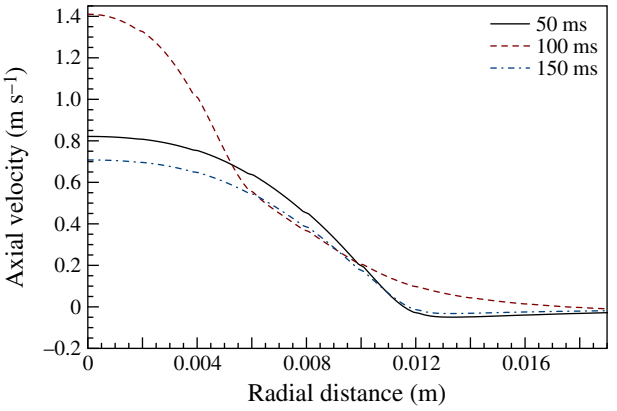


FIGURE 14. (Colour online) Axial velocity 20 mm above stagnation surface along the axes indicated in figure 13.

The first term on the right-hand side corresponds to vorticity production due to vortex stretching; the second term arises due to volumetric expansion; the third term is vorticity generation due to baroclinic torque; and the final term is viscous diffusion.

We now compute the magnitude of the different source terms in (5.2) using the simulation results for a 'puffing' flame at an equivalence ratio of $\phi = 2.5$. Since the simulations are axisymmetric, only one component of vorticity (which points out of the plane of the paper) is generated. Figure 15 shows a time-instance of the puffing motion with contours for the following terms from left to right: source term due to vortex stretching, source term due to volumetric expansion, source term due to baroclinic torque, sum of all the source terms, and the magnitude of induced vorticity. As before, the flame location is indicated by a black line corresponding to an isocontour of the progress variable. The contour plot for vorticity includes velocity vectors illustrating the direction of the flow. The source term due to diffusion is negligible and hence is not plotted here.

The vorticity is primarily generated along the flame front. The source terms due to vortex stretching and volumetric expansion along the flame front are opposite in direction to that produced by baroclinic torque. The magnitude of this last term is considerably larger (100 times) than that due to vortex stretching and volumetric expansion. The net result is a positive (anticlockwise) generation of vorticity along the vertical edges of the flame.

Neglecting all source terms but the baroclinic term in the vorticity equation (equation (5.2)), we may estimate the vorticity magnitude at the flame front:

$$u_n \frac{\partial \omega_\theta}{\partial n} \sim \frac{\partial \rho}{\partial n} \frac{\partial p}{\partial x} \frac{1}{\rho^2}, \tag{5.3}$$

where u_n is the velocity normal to the flame front, ω_θ is the vorticity out of the plane, and n is the coordinate normal to the flame front. This leads to

$$\omega_\theta = \frac{\rho_b - \rho_u}{\rho_u u_n} g = \frac{\rho_b - \rho_u}{\rho_u S_l} g \approx \left(\frac{1}{\epsilon} - 1\right) \frac{g}{S_l} \approx 200 s^{-1}, \tag{5.4}$$

with a more general analysis along these lines given in Uberoi, Kuethe & Menkes (1958). This estimate should be considered as an upper limit (as it assumes the density

https://doi.org/10.1017/jfm.2013.495 Published online by Cambridge University Press

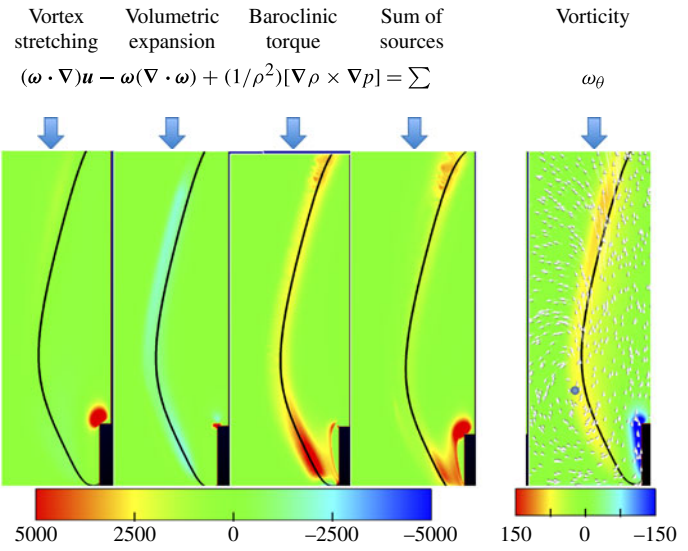


FIGURE 15. The vorticity production terms along the flame front in units of s^{-2}, and resulting out of plane vorticity, ω_θ, in units of s^{-1}, at $t = 50$ ms associated with the incipient puff. The black line corresponds to an isocontour of the progress variable at $C = 0.15$.

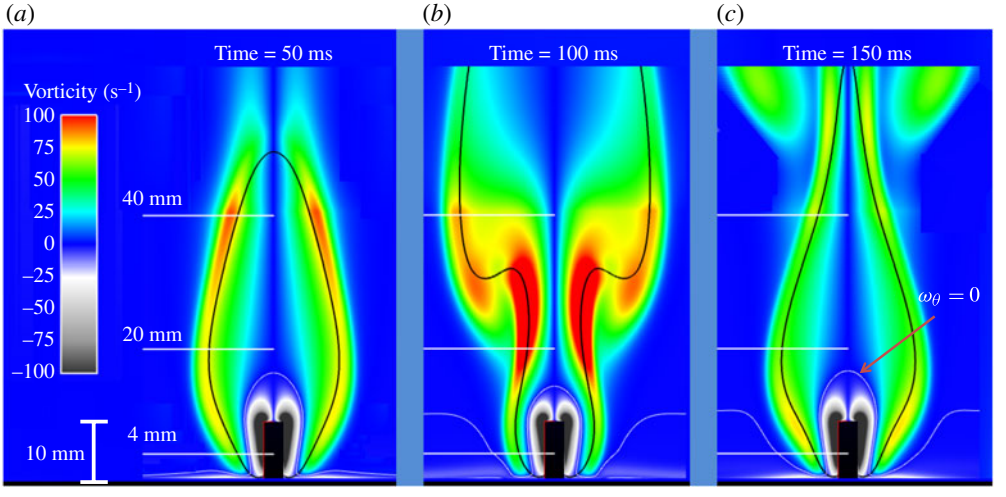


FIGURE 16. Detailed vorticity distribution at simulation time of (*a*) 50 ms, (*b*) 100 ms, and (*c*) 150 ms. The black line corresponds to an isocontour of the progress variable at $C = 0.15$. The thin white line indicates the location of the zero vorticity isocontour.

and pressure gradients are orthogonal) and is consistent with the results obtained in the simulations (figure 16).

The velocity that is induced by a vorticity distribution can be calculated using the Biot–Savart law:

$$\boldsymbol{u} = -\frac{1}{4\pi}\int \frac{\boldsymbol{s}\times\boldsymbol{\omega}(\zeta)}{s^3}\,\mathrm{d}V_\zeta. \tag{5.5}$$

https://doi.org/10.1017/jfm.2013.495 Published online by Cambridge University Press

For a cylindrical sheet of vorticity $\mathrm{d}V_\zeta = 2\pi r\,\mathrm{d}r\,\mathrm{d}z$ and along the centreline, we have $s = \sqrt{r^2 + (z - z_0)^2}$. If we consider a finite sheet of vorticity of length L, that only extends over the flame front δ_f for a flame radius R,

$$u = -\frac{1}{4\pi}\int_{-L/2}^{L/2}\int_{R}^{R+\delta_f}\frac{\omega_\theta \sin\theta}{s^2}2\pi r\,\mathrm{d}r\,\mathrm{d}z, \tag{5.6}$$

where $\sin\theta = r/s$. The integration can be carried out by noting that some terms are negligible since $\delta_f \ll R$, such that the final vorticity-induced velocity is given by

$$u = -\omega_\theta \delta_f \frac{L}{\left(4R^2 + L^2\right)^{1/2}}. \tag{5.7}$$

For a flame of 10 mm radius and with a 40 mm height the final inflow velocity using the 200 s^{-1} vorticity is 0.18 m s^{-1}, which is ∼15–20 % of the velocity observed inside the flame (see figure 14). Once again, this should be understood as an upper limit of the velocity induced by the vorticity at the flame front.

5.1.3. *Dilatation*

One way to estimate the influence of the volumetric expansion is by computing the pressure jump across the flame. In the reference frame of the flame, the unburned gases flow into the flame at a speed w_1, the laminar burning speed, and exit the flame at the flame propagation speed w_2, the product of the laminar burning speed and the expansion ratio:

$$w_1 = S_L \tag{5.8}$$

$$w_2 = \epsilon S_L. \tag{5.9}$$

Note that both w_1 and w_2 are orthogonal to the flame front. The jump relation across the flame front is

$$P_2 + \rho_2 w_2^2 = P_1 + \rho_1 w_1^2, \tag{5.10}$$

where subscript 1 represents unburned gas and subscript 2 represents burned gas. Substituting in for the velocities and densities gives the pressure jump

$$\Delta P = -\rho_u S_L^2(\epsilon - 1). \tag{5.11}$$

For a rich *n*-hexane/air ($\phi = 3.0$) flame that exhibits puffing behaviour, the initial density is ∼1.2 kg m^{-3}, the laminar flame speed is roughly 0.04 m s^{-1}, and the expansion ratio is around 5.5. Thus, the pressure jump across the flame front is ∼0.01 Pa.

In the steady flow outside the flame, the flow-induced pressure, $(\Delta P)_f$, can be estimated by considering the maximum velocity ahead of the flame. For a spherical flame, the velocity just ahead of the flame can be estimated to be

$$u(r) = (\epsilon - 1)S_L\frac{R^2(t)}{r^2}, \quad r \geqslant R, \tag{5.12}$$

where $u(r)$ is the radial velocity at a distance r from the axis and $R(t)$ is the flame radius at time t. Then, from (5.12),

$$(\Delta P)_f \sim \tfrac{1}{2}\rho u^2 \sim \tfrac{1}{2}\rho_u(\epsilon - 1)^2 S_L^2 \tag{5.13}$$

which, using the values from above, is ∼0.02 Pa.

https://doi.org/10.1017/jfm.2013.495 Published online by Cambridge University Press

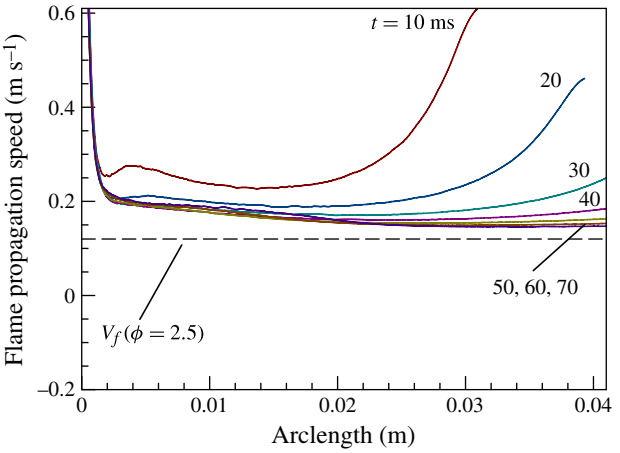


FIGURE 17. (Colour online) Flame propagation speed relative to the unburned gas along the flame front as a function of time.

Finally, these values for pressure jump across the flame front (0.01 Pa) and the flow-induced pressure (0.02 Pa) must be compared to the pressure change due to gravity. Given a 10 cm diameter flame, the hydrostatic pressure head is

$$\Delta P = \rho g d \approx 1.2 \text{ Pa}. \tag{5.14}$$

5.1.4. *Summary*

We conclude that the hydrostatic pressure head is dominant and the main mechanism responsible for creating a 'puff' is buoyancy with a lesser contribution from flame-generated vorticity (15–20 % of the observed velocity) and a negligible contribution from dilatation (60 times less than the hydrostatic pressure head).

5.2. *Onset of puffing: inflow velocity versus flame velocity*

The phenomenon ultimately responsible for the formation of a 'puff' is the competition between the inflow velocity and the flame propagation velocity. The inflow velocity and flame velocity can be extracted directly from the simulation. In figures 17 and 18, both are presented as a function of the arclength coordinate along the flame front starting at the base of the flame at the glow plug and ending at the top of the flame.

The inflow velocity, U_n, is defined as the projection of the local instantaneous velocity vector onto the flame normal, $U_n = -\boldsymbol{u} \cdot \boldsymbol{n}$. The flame propagation velocity was defined in (3.1) and corresponds to the propagation speed of the flame front in the direction normal to the flame front. The flame normal was evaluated by taking the gradient of the progress variable, $\boldsymbol{n} = \nabla C/|\nabla C|$.

Figure 17 shows the evolution of the flame propagation speed at various instances in time. The flame speed is strongly influenced by the temperature in the hot plume above the glow plug, which increases the flame speed. As the flame propagates out of the plume, the propagation speed asymptotes to a constant value comparable to the product of the laminar burning velocity, S_L, and the expansion ratio across the flame front, ϵ, $V_f = \epsilon S_L$.

As shown in figure 18, initially, the flame pushes the gases outward giving a negative inflow velocity, as shown in figure 13 on the top of the flame. Then, the flow

https://doi.org/10.1017/jfm.2013.495 Published online by Cambridge University Press

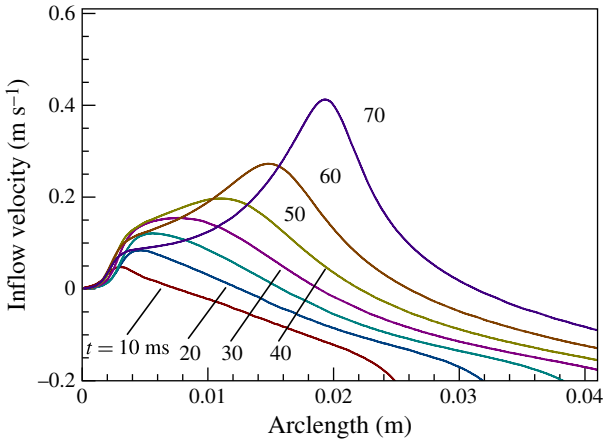


FIGURE 18. (Colour online) Inflow velocity normal to the flame front measured at different times. Positive velocities imply flow going from unburned to burned side.

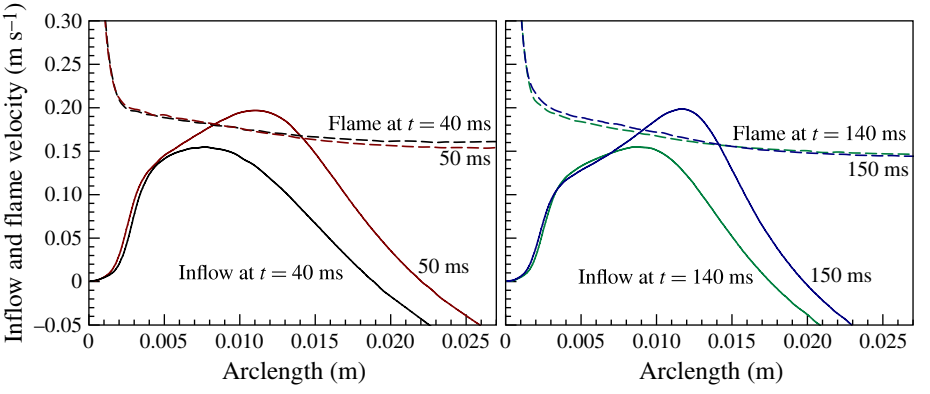


FIGURE 19. (Colour online) Inflow velocity and flame propagation velocity along the flame front as a function of time, showing period behaviour consistent with the 10 Hz frequency observed in experiments and simulations.

turns inward and gains in magnitude as shown in figure 13 at the base of the flame. This increase in inflow velocity is primarily due to the entrainment of the buoyant plume of combustion products and to a lesser extent by the continuous production of vorticity along the flame front due to baroclinic torque.

Figure 19 shows a direct comparison of the flame propagation (from figure 17) and inflow velocity (from figure 18) indicating that the cross-over point occurs between 40 and 50 ms and between 140 and 150 ms. At early times, the flame propagation speed is greater than the inflow velocity. However, as time goes by, the inflow velocity increases and the flame propagation speed decreases. At 50 ms, the inflow velocity exceeds the flame propagation velocity (figure 19). At this point, the flame moves back towards the centreline due to the flame motion relative to the incoming flow. From this point in the puffing cycle, the inflow velocity will be greater than the burning speed, until the puffing cycle is complete. The same cross-over observed between 40 and 50 ms reoccurs between 140 and 150 ms. This period is consistent with the observed 10 Hz puffing frequency. The inflow must be strong enough to exceed the

https://doi.org/10.1017/jfm.2013.495 Published online by Cambridge University Press

flame propagation to generate the periodic motion. The puff is advected upward sufficiently fast that the subsequent puff is not influenced by the previous cycle.

6. Conclusions

In this work, we have presented a combined experimental and numerical investigation of flame propagation in a premixed mixture after ignition by a hot surface. Two different regimes were observed: single flames and puffing flames. This puffing phenomenon was only observed for sufficiently large Richardson numbers. This discovery extends the range of observed puffing or flickering flames that were previously observed in non-premixed buoyant flames and premixed momentum-driven flames.

By varying the size of the hot surface, power input, and combustion vessel volume, we determined that the periodic motion is a function of the interaction of the flame with the fluid flow induced by the combustion products rather than the initial plume established by the hot surface. Further, the periodic motion is neither caused by acoustic interaction with the vessel nor by a large-scale recirculation zone. The phenomenon is accurately reproduced in numerical simulations, and a detailed flow field analysis revealed a competition between the inflow velocity at the base of the flame and the flame propagation speed. The inflow is caused mostly by the entrainment flow due to the buoyancy-induced acceleration of the light combustion products. The vorticity generated at the flame front due to baroclinic torque was found to have a secondary contribution to the inflow velocity. The inflow velocity exceeding the flame propagation speed is responsible for creating a ‘puff’. This puff is then accelerated upward, a process that is repeated periodically until the combustion vessel is filled with products.

Acknowledgements

The authors gratefully acknowledge funding for this research by the Boeing Company through Strategic Research and Development Relationship Agreement CT-BA-GTA-1.

Supplementary materials

Supplementary materials are available at http://dx.doi.org/10.1017/jfm.2013.495.

REFERENCES

BANE, S. P. M., SHEPHERD, J. E., KWON, E. & DAY, A. C. 2011 Statistical analysis of electrostatic spark ignition of lean H2/O2/Ar mixtures. *Intl J. Hydrogen Energy* **36** (3), 2344–2350.

BLANQUART, G., PEPIOT-DESJARDINS, P. & PITSCH, H. 2009 Chemical mechanism for high temperature combustion of engine relevant fuels with emphasis on soot precursors. *Combust. Flame* **156**, 588–607.

BOETTCHER, P. A. 2012 Thermal ignition. PhD thesis, California Institute of Technology.

BUCKMASTER, J. & PETERS, N. 1988 The infinite candle and its stability: a paradigm for flickering diffusion flames. In *Twenty-First Symposium (International) on Combustion*, pp. 1829–1836. Elsevier.

CETEGEN, B. M. & AHMED, T. A. 1993 Experiments on the periodic instability of buoyant plumes and pool fires. *Combust. Flame* **93** (1–2), 157–184.

CHAMBERLIN, D. S. & ROSE, A. 1948 The flicker of luminous flames. *Proc. Symp. Combust.* **1**, 27–32.

https://doi.org/10.1017/jfm.2013.495 Published online by Cambridge University Press

CHENG, R. K., BÉDAT, B. & KOSTIUK, L. W. 1999 Effects of buoyancy on lean premixed V-flames. Part I. Laminar and turbulent flame structures. *Combust. Flame* **116** (3), 360–375.

DAVIS, S. G. & LAW, C. K. 1998*a* Determination of and fuel structure effects on laminar flame speeds of C1 to C8 hydrocarbons. *Combust. Sci. Technol.* **140** (1–6), 427–449.

DAVIS, S. G. & LAW, C. K. 1998*b* Laminar flame speeds and oxidation kinetics of iso-octane–air and *n*-heptane–air flames. In *Twenty-Seventh Symposium (International) on Combustion*, pp. 521–527. Elsevier.

DESJARDINS, O., BLANQUART, G., BALARAC, G. & PITSCH, H. 2008 Higher-order conservative finite difference scheme for variable density low Mach number turbulent flows. *J. Comput. Phys.* **227**, 7125–7159.

DURAO, D. F. G. & WHITELAW, J. H. 1974 Instantaneous velocity and temperature measurements in oscillating diffusion flames. *Proc. R. Soc. Lond.* A **338** (1615), 479–501.

DUROX, D., BAILLOT, F., SCOUFLAIRE, P. & PRUD'HOMME, R. 1990 Some effects of gravity on the behaviour of premixed flames. *Combust. Flame* **82** (1), 66–74.

DUROX, D., YUAN, T. & VILLERMAUX, E. 1997 The effect of buoyancy on flickering in diffusion flames. *Combust. Sci. Technol.* **124** (1–6), 277–294.

GRAFTIEAUX, L., MICHARD, M. & GROSJEAN, N. 2001 Combining PIV, POD and vortex identification algorithms for the study of unsteady turbulent swirling flows. *Meas. Sci. Technol.* **12**, 1422–1429.

GRANT, A. J. & JONES, J. M. 1975 Low-frequency diffusion flame oscillations. *Combust. Flame* **25**, 153–160.

GUAHK, Y. T., LEE, D. K., OH, K. C. & SHIN, H. D. 2009 Flame-intrinsic Kelvin–Helmholtz instability of flickering premixed flames. *Energy & Fuels* **23** (8), 3875–3884.

HUANG, Y., SUNG, C. J. & ENG, J. A. 2004 Laminar flame speeds of primary reference fuels and reformer gas mixtures. *Combust. Flame* **139** (3), 239–251.

JI, C., DAMES, E., WANG, Y. L., WANG, H. & EGOLFOPOULOS, F. N. 2010 Propagation and extinction of premixed C_5–C_{12} *n*-alkane flames. *Combust. Flame* **157** (2), 277–287.

KELLEY, A. P., SMALLBONE, A. J., ZHU, D. L. & LAW, C. K. 2011 Laminar flame speeds of C_5 to C_8 *n*-alkanes at elevated pressures: experimental determination, fuel similarity, and stretch sensitivity. *Proc. Combust. Inst.* **33**, 963–970.

KIMURA, I. 1965 Stability of laminar jet flames. In *Tenth Symposium (International) on Combustion*, pp. 1295–1300. Elsevier.

KINT, J. H. 1970 A noncatalytic coating for platinum–rhodium thermocouples. *Combust. Flame* **14** (2), 279–281.

KOSTIUK, L. W. & CHENG, R. K. 1995 The coupling of conical wrinkled laminar flames with gravity. *Combust. Flame* **103** (1–2), 27–40.

KUMAR, K., FREEH, J. E., SUNG, C. J. & HUANG, Y. 2007 Laminar flame speeds of preheated iso-octane/O_2/N_2 and *n*-heptane/O_2/N_2 mixtures. *J. Propul. Power* **23** (2), 428–436.

LEONARD, B. P. 1979 A stable and accurate convective modelling approach based on quadratic upstream interpolation. *Comput. Meth. Appl. Mech. Engng* **19**, 59–98.

MENON, S. K., BOETTCHER, P. A. & BLANQUART, G. 2013 Enthalpy based approach to capture heat transfer effects in premixed combustion. *Combust. Flame* **160** (7), 1242–1253.

NARAYANASWAMY, K., BLANQUART, G. & PITSCH, H. 2010 A consistent chemical mechanism for oxidation of substituted aromatic species. *Combust. Flame* **157** (10), 1879–1898.

OIJEN, J. A. VAN & DE GOEY, L. P. H. 2000 Modelling of premixed laminar flames using flamelet-generated manifolds. *Combust. Sci. Technol.* **161**, 113–137.

PALM-LEIS, A. & STREHLOW, R. A. 1969 On the propagation of turbulent flames. *Combust. Flame* **13** (2), 111–129.

PETERS, N. 1988 Laminar flamelet concepts in turbulent combustion. *Twenty-First Symposium (International) on Combustion* 1231–1250.

PIERCE, C. D. 2001 Progress-variable approach for large-eddy simulation of turbulent combustion. PhD thesis, Stanford University.

PIERCE, C. D. & MOIN, P. 2004 Progress-variable approach for large-eddy simulation of non-premixed turbulent combustion. *J. Fluid Mech.* **504** (1), 73–97.

https://doi.org/10.1017/jfm.2013.495 Published online by Cambridge University Press

SHEN, H. P. S., STEINBERG, J., VANDEROVER, J. & OEHLSCHLAEGER, M. A. 2009 A shock tube study of the ignition of *n*-heptane, *n*-decane, *n*-dodecane, and *n*-tetradecane. *Energy Fuels* **23**, 2482–2489.

SHEPHERD, I. G., CHENG, R. K. & DAY, M. S. 2005 The dynamics of flame flicker in conical premixed flames: an experimental and numerical study. *Tech. Rep.* LBNL-59249, Lawrence Berkeley National Laboratory.

SIVASHINSKY, G. I. 2002 Some developments in premixed combustion modelling. *Proc. Combust. Inst.* **29** (2), 1737–1761.

STRAWA, A. & CANTWELL, B. 1989 Investigation of an excited jet diffusion flame at elevated pressure. *J. Fluid Mech.* **200**, 309–336.

TANOUE, K., OGURA, Y., TAKAYANAGI, M. & NISHIMURA, T. 2010 Measurement of temperature distribution for the flickering phenomenon around the premixed flame by using laser speckle method. *J. Visual.* **13** (3), 183–185.

TOONG, T., SALANT, R. F., STOPFORD, J. M. & ANDERSON, G. Y. 1965 Mechanisms of combustion instability. In *Tenth Symposium (International) on Combustion*, pp. 1301–1313. Elsevier.

TRAN, L. S., GLAUDE, P. A. & BATTIN-LECLERC, F. 2013 Experimental study of the structure of laminar premixed flames of ethanol/methane/oxygen/argon. *Combust. Explos. Shock Waves* **49**, 11–18.

UBEROI, M. S., KUETHE, A. M. & MENKES, H. R. 1958 Flow field of a Bunsen flame. *Phys. Fluids* **1** (2), 150–158.

VAN LIPZIG, J. P. J., NILSSON, E. J. K., DE GOEY, L. P. H. & KONNOV, A. A. 2011 Laminar burning velocities of *n*-heptane, iso-octane, ethanol and their binary and tertiary mixtures. *Fuel* **90**, 2773–2781.

WANG, H., DAMES, E., SIRJEAN, B., SHEEN, D. A., TANGKO, R., VIOLI, A., LAI, J. Y. W., EGOLFOPOULOS, F. N., DAVIDSON, D. F., HANSON, R. K., BOWMAN, C. T., LAW, C. K., TSANG, W., CERNANSKY, N. P., MILLER, D. L. & LINDSTEDT, R. P. 2010 A high-temperature chemical kinetic model of *n*-alkane (up to *n*-dodecane), cyclohexane, and methyl-, ethyl-, *n*-propyl and *n*-butyl-cyclohexane oxidation at high temperatures. JetSurF version 2.0, September 19, 2010.

WESTBROOK, C. K., PITZ, W. J., HERBINET, O., CURRAN, H. J. & SILKE, E. J. 2009 A detailed chemical kinetic reaction mechanism for *n*-alkane hydrocarbons from *n*-octane to *n*-hexadecane. *Combust. Flame* **156**, 181–199.

WYZGOLIK, A. & BAILLOT, F. 2008 Non-premixed lifted flame stabilization coupled with vortex structures in a coaxial jet. *Combust. Sci. Technol.* **180**, 1956–1971.

ZABETAKIS, M. G. 1965 Flammability characteristics of combustible gases and vapours. Bulletin 627, Bureau of Mines.

ZUKOSKI, E. E. 1986 Fluid dynamic aspects of room fires. In *Proceedings of First International Symposium Fire Safety Science*.

https://doi.org/10.1017/jfm.2013.495 Published online by Cambridge University Press